

Supporting Information for “Eigenmode Tomography of Surface Charge Oscillations of Plasmonic Nanoparticles by Electron Energy Loss Spectroscopy”

Sean M. Collins,[†] Emilie Ringe,[‡] Martial Duchamp,[§] Zineb Saghi,[†] Rafal E. Dunin-Borkowski,[§] and Paul A. Midgley[†]

[†]*Department of Materials Science and Metallurgy, University of Cambridge, 27 Charles Babbage Road, Cambridge, CB3 0FS, United Kingdom*

[‡]*Department of Materials Science and Nanoengineering, Rice University, 6100 Main Street MS-325, Houston, Texas 77005-1827, USA*

[§]*Ernst Ruska-Centre for Microscopy and Spectroscopy with Electrons and Peter Grünberg Institute, Forschungszentrum Jülich, D-52425 Jülich, Germany*

This supporting information file contains additional data and discussion referenced in the main text pertaining to the methods, analysis and non-negative matrix factorization (NMF) decomposition of experimental scanning transmission electron microscopy electron energy loss spectroscopy (STEM-EELS) of silver right bipyramids, boundary element method (BEM) simulations of spectra and loss probability maps, mesh generation for BEM simulations, eigenmode calculations, validation of surface charge reconstructions, and surface charge reconstructions of edge and face modes.

Extended Methods

Spectral Processing. After spike-removal due to x-rays striking the charge-coupled device detector, spectra were aligned to the zero loss peak (ZLP) using two different methods for plan-view and combined tilt-series data sets. For plan-view spectrum images, the spectra were immediately aligned to sub-pixel accuracy using a correlation routine using the ZLP. For tilt-series data, the spectra were first aligned to the ZLP by identifying the maximum intensity channel and shifting spectra to the energy zero. The spectrum images were then combined for simultaneous processing, and the ZLP alignment was performed to sub-pixel accuracy using the correlation-based routine on all tilt-series spectrum images at once.

In order to identify an appropriate number of components, decompositions were repeated in each case using a range of different components. For tilt-series data, the number of tilts used in the decomposition was also varied. In using a decomposition approach like NMF, the effect of

contamination is readily apparent when an additional component is required to represent the data. NMF decomposition required a distinct component for the first pristine tilt (0°) for the lowest energy mode, attributed to a shift in the energy of the lowest energy resonance mode following acquisition of the first map and concomitant electron-beam induced carbon contamination (see also Fig. S13). Unfortunately, due to the probable oxidation of silver, conventional plasma cleaning to remove carbon (Ar/O₂ plasma) was not possible prior to electron beam exposure. As a further assessment of the number of components to retain in the decompositions, principal-component analysis (PCA) scree plots were also examined, giving similar results.

As noted in previous work,¹ the EELS signal is a good approximation to the single scattering distribution. The EELS signal is therefore proportional to the product of scattering by the surface plasmon resonance and the area of the ZLP. The component maps shown in Fig. 1-2 are not corrected for this ZLP dependence due to the poor signal-to-noise for penetrating trajectories. For comparison with simulations, external (non-penetrating) trajectories are unaffected as the ZLP is approximately constant for all pixels outside the particle. For surface charge reconstructions, the selected non-penetrating trajectories were divided by the ZLP signal pixel-by-pixel to account for this necessary quantitative correction.

Surface charge reconstructions. Here we expand in greater detail on the method proposed by Hörl et al.² and identify extensions to the method for handling noisy experimental data (regularization). Alternative methods for the qualitative reconstruction of EELS of surface plasmons have been demonstrated previously,¹ and new theoretical proposals for reconstruction of the dyadic Green's tensor from EELS are forthcoming.³ The presented surface charge tomography realizes a first experimental demonstration of quantitative and direct reconstruction of eigenmodes. To summarize the surface charge reconstruction method, equation (1) establishes the loss probability in the quasi-static approximation as a summation over eigenmodes k . If a surface element discretization is employed, the calculated energy loss corresponding to a single mode is then

$$\Gamma_k^{\text{EELS}}(\mathbf{R}_0) = A_k \left| \sum_s a_s \phi_{\mathbf{R}_0,s}^* \sigma_{k,s} \right|^2 \quad (\text{S1})$$

where the expression is now at fixed ω , corresponding to the on-resonance amplitude for experimental data, a_s is the surface element area, and the subscripts s denote the surface elements.

A_k is a frequency dependent coefficient for mode k . Equation (S1) is then used to compute Γ^{calc} in equation (2). Even with the elimination of penetrating trajectories, equation (2) remains an overdetermined problem where solutions can be found through approaches such as conjugate-gradient minimization routines.² The subscripts k are eliminated in the following treatment for simplicity in discussing reconstructions for a single mode k .

The optimization problem in equation (2) can be written explicitly as the cost function²:

$$J = \sum_{n=1}^{N_{pix}} \frac{1}{2} |\Gamma_n^{exp} - \Gamma_n^{calc}|^2 \quad (S2)$$

where n specifies a pixel in the EELS spectrum image (i.e. a particular trajectory). The cost function J is then minimized by the conjugate gradient solver.

In order to efficiently compute the gradient, the analytical gradient of the cost function was determined using the relation:

$$\frac{\partial}{\partial \sigma_s} J = \sum_{n=1}^{N_{pix}} (\Gamma_n^{exp} - \Gamma_n^{calc}) \times \left(-2A \left[\text{Re}\{C_{ns}\} \sum_{s'} \text{Re}\{C_{ns'}\} \sigma_{s'} + \text{Im}\{C_{ns}\} \sum_{s'} \text{Im}\{C_{ns'}\} \sigma_{s'} \right] \right) \quad (S3)$$

where C_{ns} is a matrix element given in terms of the area element and the trajectory-specific potential ϕ defined as $C_{ns} = a_s \phi_{ns}^*$ where now n denotes the pixel trajectory given by the coordinate \mathbf{R}_0 in equation (S1) and A is a constant as given in equation (3).

In order to avoid over-fitting to the noise present in the experimental data, equation (2) was modified with the addition of a regularization term as in equation (3). Tikhonov regularization, for example, employs:

$$\|F(\hat{\sigma})\|_2^2 = \|\hat{\sigma}\|_2^2 \quad (S4)$$

Such a regularization term minimizes large jumps in the solution and can improve algorithmic stability. However, Tikhonov regularization favors relatively flat solutions in terms of surface charge magnitudes, a property not reflected in eigenmode surface charge distributions as presented in Fig. 5.

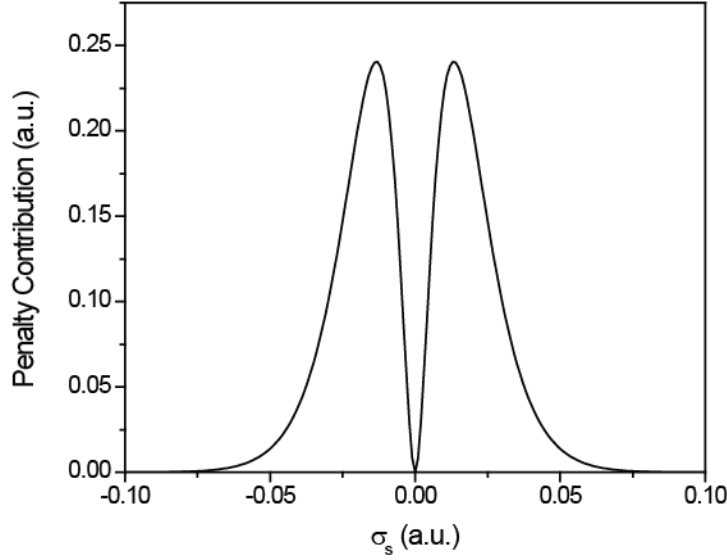


Figure S1 | Illustration of penalty contribution to the regularization term in surface charge tomography (equation (3)-(4)). The γ parameter is set to 150 and the intensity, controlled by λ , is plotted on a convenient scale.

In the case of corner modes, a few surface elements are highly charged and the remainder are near zero charge. As such, $F(\hat{\sigma})$ was selected as a soft thresholding operator to promote solutions of this kind. A suitable regularization operator for ℓ_2 -minimization using the conjugate gradient method should be differentiable and also account for the structure of the surface charge distribution of plasmonic eigenmodes. A thresholding operator was written to satisfy these requirements in the form of equation (4). The contributions of different values of σ_s to the thresholding operator defined in equation (4) are plotted in Fig. S1 for reference. In equation (4), at small values of σ_s where $e^{-\gamma|\sigma_s|} \approx 1$, equation (4) results in the same regularization weighting as in equation (S4). At larger values, surface charges above a soft threshold determined by the tail of the exponential (set by γ) are minimally penalized in this regularization scheme. Consequently, only large charge density values are promoted in the solution by the regularization term and so the total minimization scheme using equation (3) finds solutions consistent with the experimental data that also exhibit high surface charge values. The data fidelity term (cost

function J) guides these high surface charge values to the spatial surface regions appropriate to each respective mode.

Weighting factors were selected by repeating the optimization for a range of values. L-curve plots for optimal selection of the weighting factors by inspection of the dependence of the solution norm and residual norm as a function of weighting parameters were examined but did not exhibit a clear rectifying feature.⁴ By examining the effects of the weighting factors across a range of values, weighting factors were ultimately selected for the minimum weighting required to remove spurious high frequency surface charge oscillations from the reconstructions.

In order to use the NMF component map data with the reconstructed surface mesh, a coordinate alignment was performed in MATLAB using coordinate transformation and image registration routines. Because the trajectory coordinate \mathbf{R}_0 is the only parameter necessary to link Γ^{calc} to Γ^{exp} , the spectrum image pixels were not transformed. Rather, the coordinates of the mesh-registered pixels were identified. A set of masks was extracted from HAADF micrographs to exclude penetrating trajectories. The masks were applied to the registered coordinates and the non-penetrating experimental trajectories. These coordinates were then used to calculate the necessary coefficient matrix elements C_{ns} using MNPBEM. Finally, the masked coefficient matrix and masked experimental trajectories were exported for use in SCIPY for reconstruction using the non-linear conjugate gradient algorithm to recover the surface charge vector. This coordinate registration process was critical for the experimental implementation of the reconstruction method proposed in Ref. ², and precise alignments were necessary for valid reconstructions from experimental data.

To initialize the reconstruction procedure, an initial guess was required for each mode. The prior knowledge of the particle morphology from electron tomography was used to estimate eigenmodes of the isolated bipyramid, analogous to those presented in Fig. 4, for the particular reconstructed surface mesh using MNPBEM. These single particle eigenmodes were used as the initial guesses for each of the modes in Fig. 5. Due to imperfections in the reconstructed surface mesh (see BEM Simulations below), higher order edge and face eigenmodes were not directly calculated from BEM. Rather, initial reconstructions from simulated retarded BEM maps were used to produce initial guesses to refine against experimental data.

The value of A_k , a constant for a single amplitude map, are in principle calculable for a known dielectric function and environment. Because these were not directly measured for the

experimental case, values of A_k were fixed by initially minimizing the cost function with the charge distribution of the initial guess fixed. Then for the fixed value of A_k the surface charge vector was refined. Results did not vary significantly for choice of A_k and it is clear from equation (S1) that they should not. The exact value of A_k corresponds to a particular units system in equation (S1). The units of surface charge were not constrained during the optimization procedure, and so the optimization procedure allows for the magnitudes to be adjusted to match experimental data. Moreover, as has been noted in previous work, NMF decomposition gives component intensities which are not relatively calibrated.¹ Leaving the surface charge units unconstrained was therefore necessary for valid reconstructions. The modes are in turn plotted on normalized scales in Fig. 5. The choice of A_k was selected to match the initial guess in order to minimize the number of iterations necessary to adjust the surface charge magnitudes in line with experimental data. For a convergence criterion of minimizing the norm of the gradient below 1×10^{-5} and optimized regularization parameters, approximately 200-500 iterations were required for convergence for the single mode reconstructions and 1000 iterations were required for the two-fold reconstruction of the $\beta_2 + \gamma$ component. This procedure in turn resulted in a decrease in the value of the cost function typically of the order of a 10-fold reduction. The relative reduction in the cost function intrinsically depends on the choice of the initial guess, and so the norm of the gradient is a more suitable convergence criterion.

For frequencies in the spectrum where multiple modes contribute, such as for the $\beta_2 + \gamma$ component and for the edge mode series (δ), equation (S1) can be extended as a partial, but truncated, sum over two or more eigenmodes:

$$\Gamma^{calc} = \sum_{k=k_1}^{k_2} A_k \left| \int da \phi^* \sigma_k(\mathbf{s}) \right|^2 \quad (\text{S5})$$

where now for each mode k there are distinct $\sigma_k(\mathbf{s})$. In Fig. 5, the $\beta_2 + \gamma$ component was reconstructed as two simultaneous reconstructions using equation (S5). The weighting factors A_k were set, as a coarse approximation, to being equal in order to avoid input bias in the reconstruction. Critically, the units of $\sigma_k(\mathbf{s})$ are not constrained during optimization, and so the magnitudes of the charges are adjusted during the conjugate gradient optimization procedure allowing the charge reconstruction to match the weights of the respective mode contributions to

the experimental data. The reconstructions are ultimately presented on a normalized scale to equalize the units across each of the mode reconstructions.

To examine the effects of contamination on the experimental NMF components, the non-penetrating trajectories used for reconstruction were re-calculated using BEM simulations. Comparison at each tilt used for reconstruction indicated systematic discrepancies in the intensities for the two lowest-energy modes. Weighting factors were assessed as constant multipliers for each tilt, and reconstructions with and without re-weighting the intensities to correspond to the simulation data produced similar results. The reconstructions with re-weighting showed reduced scatter in the reconstructed surface charges and are therefore shown in Fig. 5.

To further assess the validity of the reconstructions, re-calculated loss probability maps from the reconstructed surface charge vectors were compared with the experimental maps and are presented in Fig. S15. Additionally, maps of the data fidelity term J are presented in Fig. S16. In tomographic reconstructions it is also common practice to investigate the reconstruction procedure for a phantom data-set. By analogy, reconstructions using retarded BEM simulations as the input data (I^{exp}) are presented in Fig. S21-23. The phantom reconstructions serve to demonstrate the reconstruction method without artefacts from NMF decomposition, contamination, or experimental noise. Phantom reconstructions show good correspondence with experimental reconstructions for the same initial guess and regularization procedures.

HAADF Tomography. Electron tomography was performed using a tilt-series of HAADF micrographs in order to reconstruct the particle surface, necessary to define the surface used in the surface charge reconstructions. The HAADF micrographs were initially aligned using cross-correlation techniques in INSPECT 3D (FEI) software and subsequently checked tilt-by-tilt using the Midas tool in IMOD (University of Colorado) software. The tilt-axis was then aligned in INSPECT 3D. The tilt-axis alignment was refined by examining artefacts in simultaneous iterative reconstruction technique (SIRT) reconstructions in INSPECT 3D. After the tilt-axis was aligned, a compressed sensing reconstruction algorithm⁵ was used to obtain a reconstructed volume.

Compressed sensing electron tomography (CS-ET) has been described in detail previously,^{5,6} but the key principles of the approach are discussed briefly. The concept of “compressibility” derives from the property that many signals can be represented by only a few coefficients in some transform domain. As only these coefficients need to be retained to reconstruct the entire

signal with reasonable fidelity, much less information can be stored. This idea of compression underpins image compression methods such as the JPEG file format. Compressed sensing makes use of the compressibility of signals, not after acquisition as in saving a JPEG file, but incorporates the compressibility into the signal acquisition scheme. The acquisition in turn seeks to identify a small number of coefficients from an under-sampled data set that describe the true signal with high fidelity. This approach uses a small number of “incoherent” samples; that is, the effects of limited sampling must only produce artefacts that are noise-like. Using the prior information that the signal may be represented sparsely (i.e. with a few coefficients) in a particular transform domain, a non-linear optimization approach can be applied to identify those coefficients.

In the case of CS-ET, the signal is acquired as a radial sampling of Fourier space, a signal that has been determined to be sufficiently incoherent for compressed sensing.^{7,8} The CS-ET reconstruction can then be given in terms of the minimization problem:

$$\hat{x} = \arg \min_{\hat{x}} \{ \|Fx - y\|_2^2 + \lambda \|\Psi x\|_1 \} \quad (\text{S6})$$

where \hat{x} is the vector describing the 3D reconstruction, F is the undersampled Fourier operator, y is the vector describing the Fourier transform of HAADF micrographs, ψ is the transform operator for the sparse representation domain, and λ is a weighting factor on the regularization term, comparable to the weighting of the regularization term in the surface charge tomography problem (the regularization term is the ℓ_1 -norm in the case of CS-ET).

The first term is given in terms of the ℓ_2 -norm of the difference between the reconstruction and acquired experimental data, acting as a data fidelity term. The ℓ_2 -norm is:

$$\|x\|_2 = \left(\sum_i |x_i|^2 \right)^{1/2} \quad (\text{S7})$$

where the sum is over all vector elements i . The ℓ_1 -norm is in turn:

$$\|x\|_1 = \sum_i |x_i| \quad (\text{S8})$$

The ℓ_1 -norm regularization term promotes the identification of a sparse solution⁹ when combined with the data fidelity term in equation (S6). The optimization problem seeks to find the

sparsest solution in the transform domain that is consistent with the data, the experimental HAADF micrographs in this case, or more precisely their Fourier transform. For the HAADF CS-ET reconstruction, a combination of image-domain sparsity and gradient-domain (total variation) sparsity were selected as the particle is an isolated object exhibiting sharp boundaries and uniform density.⁵

After reconstruction of the sample volume using CS-ET, the volume was segmented and the surface of the segmented particle volume was then extracted by applying a convex-hull routine in AVIZO FIRE. Due to truncation of the substrate in the HAADF tilt-series, the substrate slab was added to the reconstruction volume as a sub-volume defined geometrically by defining four planes at the boundary of the substrate. The slab was added to the reconstruction volume in MATLAB (Mathworks) software and updated iteratively to match Radon projections of the reconstruction volume. The surfaces of the particle and substrate were then re-extracted in AVIZO FIRE and then re-meshed using a multi-level meshing routine. The surface mesh was then exported to MATLAB for use with the open-source MNPBEM software.¹⁰

BEM Simulations. For the construction of surface meshes, the ideal bipyramid geometry was initially defined by calculating the volume of a thermodynamic bipyramid using a MATLAB code for a modified Wulff construction of twinned nanoparticles.¹¹ The volume of the bipyramid was scaled to represent a bipyramid with 50 nm side length (distance from 90° corner to adjacent corner for a plan-view bipyramid). For the simulations in Fig. 1, a substrate in the form of a 10 nm thick circular disk of 70 nm radius was added to the volume in contact with the bipyramid. The volume was then imported to AVIZO FIRE for mesh generation. An isolated bipyramid mesh was generated for initial BEM simulations of energy-loss spectra (Fig. S5). For Fig. 1, a multi-level meshing routine was employed as for the tomographic reconstruction volume. For the isolated bipyramid in Fig. 4, additional smoothing operations were performed on the Wulff-constructed bipyramid to ensure optimized compatibility with MNPBEM. MNPBEM routines, particularly for eigenmode calculations, were found to return artefact-free results for smooth and finely meshed surfaces. Surface meshes are presented at multiple orientations in Fig. S9 and S10 for reference.

Plan-view Bipyramids: NMF Decomposition

In order to corroborate the NMF decomposition presented in Fig. 1, Figure S2 presents minimally processed EEL spectra from selected key trajectories of the plan-view bipyramid. Spectra were aligned to the ZLP and x-ray spikes were removed, but no decomposition was performed on these spectra. The features identified in the NMF decomposition corresponding to the signatures labeled α , β_1 , β_2 , γ , δ , and ε are observed in the selected area spectra. There is significant peak overlap observable in the selected area spectra, and peak maxima are not precisely identifiable due to the strong ZLP background. Each of the modes is, however, strongly excited at the trajectories expected from the NMF component maps for the component and the BEM simulations presented in Fig. 1.

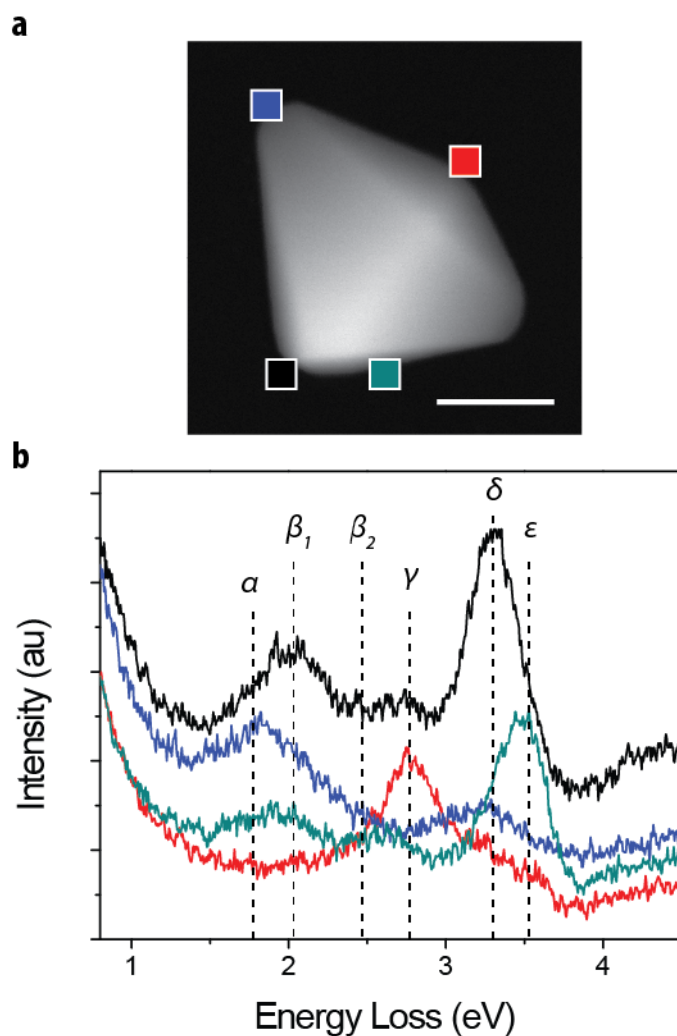


Figure S2 | Selected-area spectra of a silver right bipyramid (Fig. 1). **a**, HAADF micrograph with marked selected-area regions. The scale bar is 25 nm. **b**, Corresponding spectra from 4 key regions (9x9 pixels). The peak locations matching component features in Fig. 1 are marked with the equivalent Greek letter.

Figure S3 presents three additional NMF component maps presented in the spectral signatures depicted in Fig. 1a but not shown in Fig. 1b. The ZLP component shows high intensity evenly outside the particle as expected. The ζ component exhibits strong signal inside the particle, similar to the HAADF micrograph. This signature was attributed to the bulk plasmon mode for silver and therefore shows similar mass-thickness contrast as the HAADF micrograph. The final η component predominantly shows spectral signal at the expected MoO_3 band edge near 3.5 eV (Fig. 1a). There is additional signal along the edges, faces, and 90° corner

of the plan-view bipyramid. These signals were attributed to incomplete separation of this final spectral signature just resolved above the experimental noise level. Satellite peaks in the η are present in the vicinity of the β_2 and the δ and ε features giving rise to partial intensity in the η component map. For the low intensity MoO₃ band edge signal observed in the spectral signature, the satellite peaks are of comparable magnitude for this component and therefore significantly impact the η map. These satellite peaks do not represent a significant decrease in the signal recovered in the other modes. Along the 90° corner in Fig. 1, the η component, for example, is only weakly contributing to the total spectrum other than at energies above 3.5 eV.

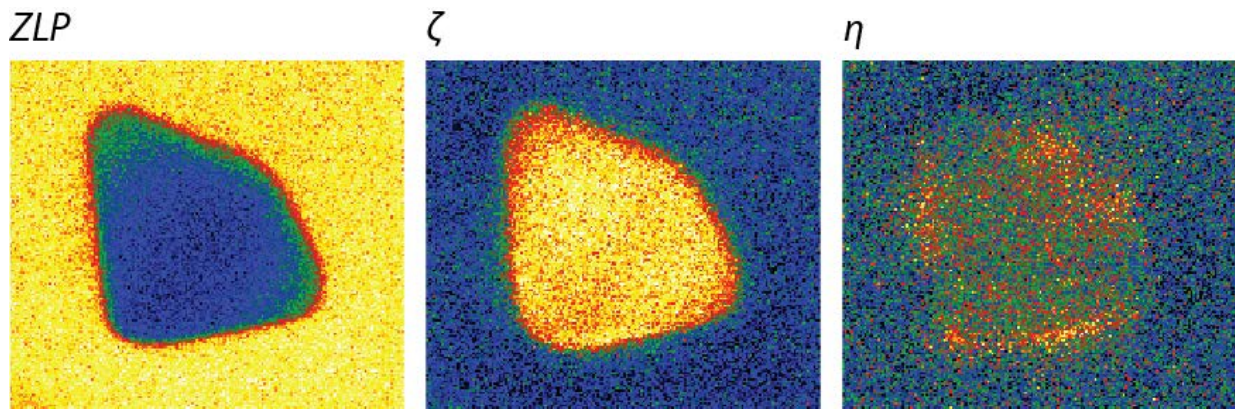


Figure S3 | Additional NMF components in Fig. 1 decomposition. The zero loss peak component (*ZLP*) corresponds to the gray line in Fig. 1. The components corresponding to the bulk (ζ) and a noise component containing spectral signatures related to the MoO₃ band edge (η) are also shown.

Figure S4 presents NMF decomposition component maps for a second plan-view silver bipyramid. The γ , δ , and ε components closely resemble those in Fig. 1 and the corresponding BEM simulation loss probability maps. The simulated maps are identical to those in Fig. 1. The α , β_1 , and β_2 components are identifiable in the data set for this second bipyramid as well. However, here α and β_1 are unseparated and β_2 is a distinct component in the NMF decomposition. Given that the α and β_1 components derive from a degenerate pair of modes (see Fig. 4 and Fig. S5, S7), regions with a thinner substrate are expected to give rise to reduced energy-splitting as a consequence of degeneracy breaking. The two nearly degenerate components are likely not resolved sufficiently in the experimental data for NMF to separate the features. Inspection of HAADF micrographs supports this interpretation that the bipyramid in Fig. S4 was located on a thinner MoO₃ crystal.

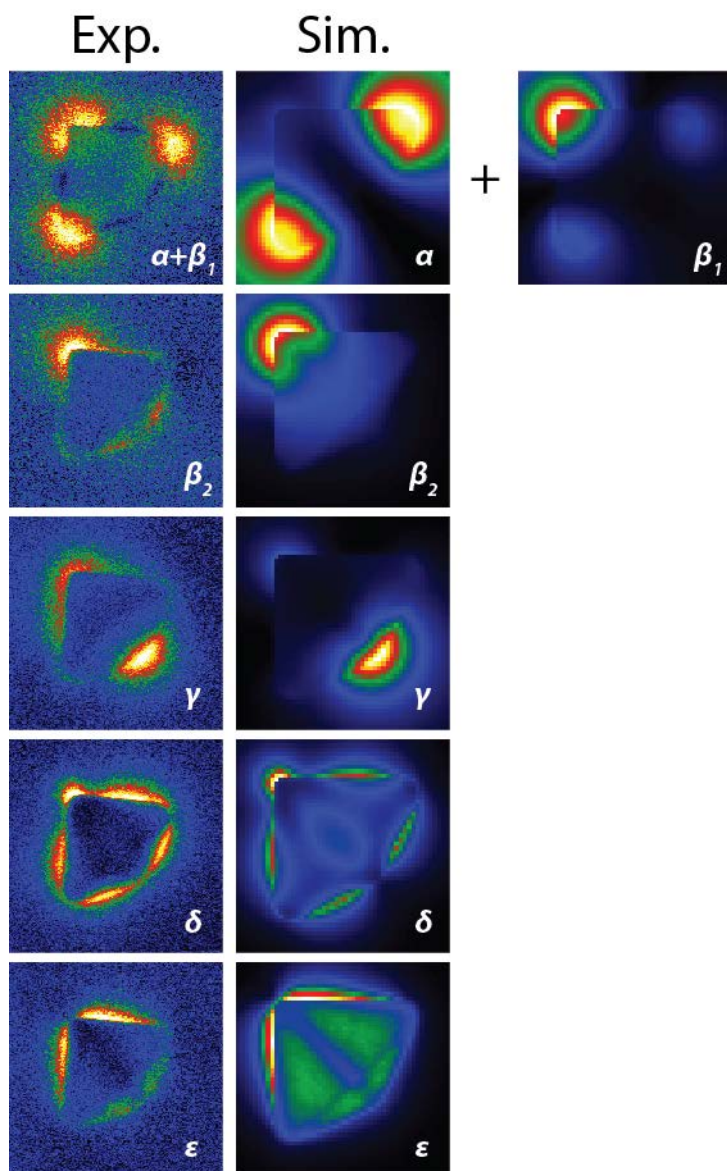


Figure S4 | Plan view EELS spectrum imaging of an additional Ag right bipyramid. NMF component maps (Exp.) and the corresponding simulated loss probability maps (Sim.) are shown. The common set of Greek letters mark the corresponding features recovered by NMF decomposition of experimental spectrum imaging and simulated maps for a thermodynamically ideal bipyramid. The components α and β_1 were separated by NMF for this bipyramid.

BEM Simulations

Figures S5-S7 present further simulations to describe the separate effects of retardation and the dielectric substrate. In Fig. S5, selected trajectory spectra for an isolated bipyramid are shown for quasi-static and fully retarded simulations. In MNPBEM, quasi-static equations are written in terms of surface charges only whereas retarded simulations account for the dynamic interaction of the excitation field (electron trajectory) and calculate induced currents and charges, or correspondingly scalar and vector potentials.¹⁰ Retardation red-shifts mode energies for increasing particle size.¹² Effectively, the quasi-static limit is obtained for small particles. This red-shift is observed in Fig. S5b. The red-shift, or reduction in energy, is not equal for all modes with greater change in energy for lower energy modes. The E' peak (see Fig. 4 and Fig. S14) is shifted most when retardation is accounted for in the case of 50 nm bipyramids examined here. The retardation effect is relatively minor for particles of this size. The use of quasi-static equations for the modal reconstruction is therefore a reasonable approximation for this particular particle size.

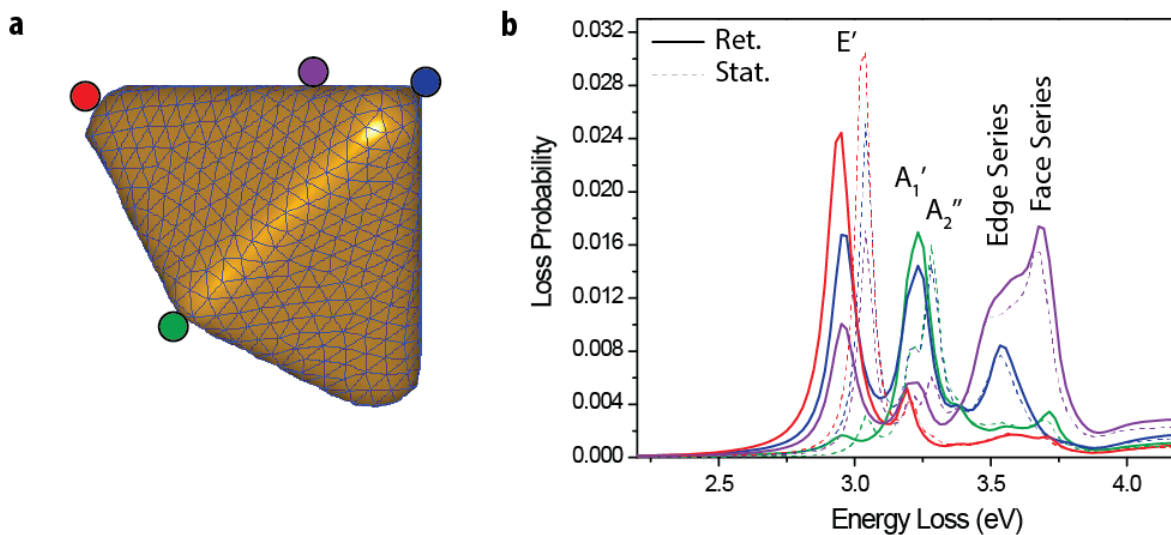


Figure S5 | Selected-trajectory spectra for a thermodynamic bipyramid. a, The surface mesh and selected trajectories. **b,** Spectra with retardation effects (solid lines) and in the quasi-static approximation (dashed lines) for the 4 trajectories in **a**. Symmetry labels are assigned for the corner modes. Line colors correspond to the trajectory colors in **a**.

The spectra in Fig. S5 also correspond exactly to the modal expansion presented in Fig. 4 whereas the modal equations do not precisely describe the retarded simulations. Figure S5 consequently also confirms that the mode structure is not significantly altered by retardation effects. The same number of modes exhibiting similar relative intensities is observed in each case.

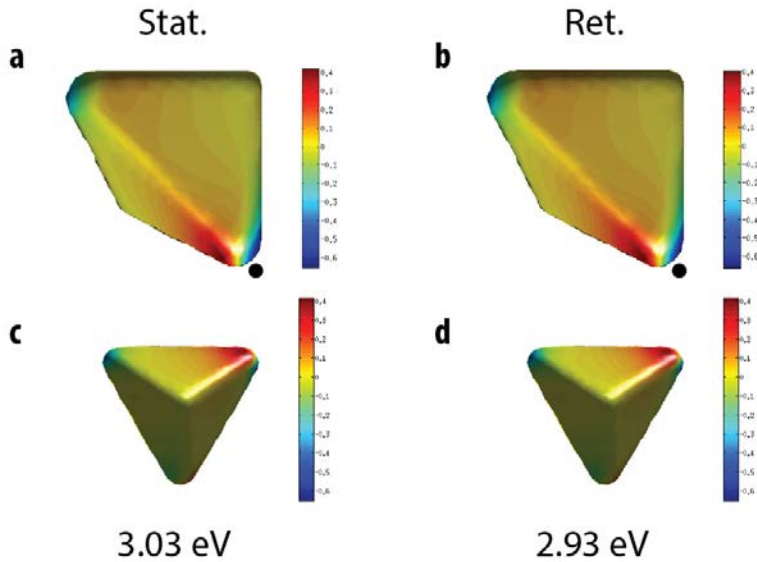


Figure S6 | Induced electric fields on the exterior of the particle surface shown at two orientations. **a,c** Electric fields calculated in the quasi-static approximation. **b,d** Electric fields calculated in with retardation effects (charges and currents). The intensity is plotted on a normalized color scale from -0.6 to 0.4 (normalized by dividing by the maximum field). The calculations were performed on the dipole resonance energy at 3.03 eV and 2.93 eV for quasi-static (Stat.) and retarded (Ret.) simulations, respectively. Black dots mark the electron trajectory in the plan view orientation.

Figure S6 presents further simulations to support the similarity in the optical response described by the quasi-static and fully retarded descriptions of the bipyramid. Electric fields at the particle surface were calculated at the lowest-energy dipolar mode, red-shifted by 0.1 eV with retardation effects included. In BEM, surface currents as well as surface charges are included in retarded simulations. Despite observable shift in mode energy due to retardation, the induced electric fields are indistinguishable for the quasi-static and retarded simulations in Fig. S6. The quasi-static approximation and its associated eigenmode expansion formalism provide a quantitative description of the optical response properties in the case of a 50 nm bipyramid.

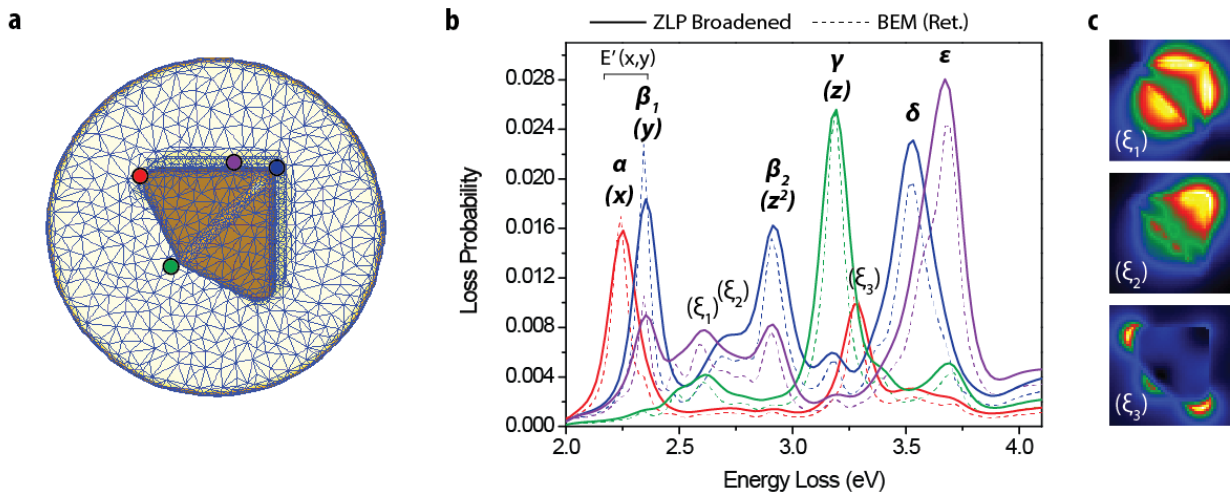


Figure S7 | Selected-trajectory spectra for a thermodynamic bipyramid on a 10 nm thick dielectric substrate. **a**, The surface mesh and selected trajectories. **b**, Spectra (with retardation) at the 4 trajectories. The effect of ZLP broadening is highlighted (solid lines). Line colors correspond to the trajectory colors in **a**. The symmetry label $E'(x,y)$ refers to the substrate-induced symmetry breaking of the degenerate E' dipole mode. **c**, Loss probability maps for additional features arising in the substrate simulation (ξ). The maps are normalized to enhance the contrast in these weak spectral features.

Substrate effects are examined in Fig. S7. Here, to match experimental conditions as closely as possible, retarded simulations were employed (as in Fig. 1 and Fig. 2). Figure S7 also presents spectra with the effects of ZLP broadening. In the EELS experiment, the spectra are convoluted with the intensity distribution of the ZLP. The highest intensities of the ZLP can be approximated by a Gaussian function, and so the broadened spectra in Fig. S7 were calculated using a Gaussian ZLP of 90 meV full-width half maximum. Figure S7 shows substrate-induced symmetry breaking and degeneracy lifting of the $E'(x,y)$ dipoles to give rise to the α and β_1 spectral features mapped in Fig. 1. In addition to the principle modes observed in Fig. S5 and in experimental NMF decomposition (α - ϵ), a few additional minor peaks are observed in the BEM simulation with the finite substrate shown in Fig. S7a. These are labeled as ξ_{1-3} . Maps for these three peaks are shown in Fig. S7c. These are weak modes not observed experimentally, and can be attributed to coupling effects with the approximate finite substrate. Imperfections in the mesh used at the interface may also give rise to non-physical modes. These signatures are not expected to significantly affect the principle mode maps which show good correspondence with the

expected eigenmodes of a bipyramid (Fig. 4) and the experimentally recovered spectral signatures.

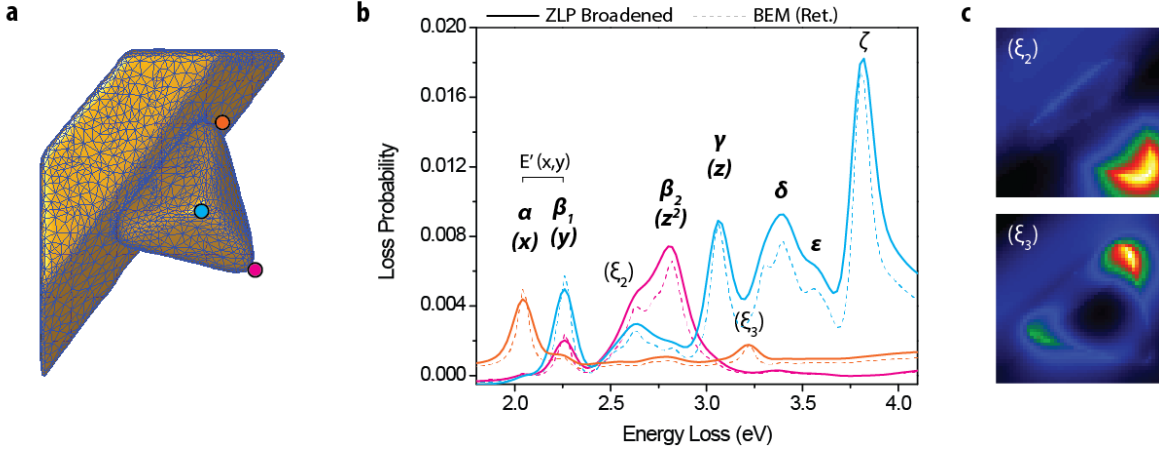


Figure S8 | Selected-trajectory spectra for the tomographically reconstructed bipyramid on a truncated dielectric substrate. a, The surface mesh and selected trajectories. **b,** Spectra (with retardation) at the 3 trajectories. The effect of ZLP broadening is highlighted (solid lines). Line colors correspond to the trajectory colors in **a**. The symmetry label $E'(x,y)$ refers to the substrate-induced symmetry breaking of the degenerate E' dipole mode. **c,** Loss probability maps for additional features arising in the substrate simulation (ξ). The maps are normalized to enhance the contrast in these weak spectral features.

Figure S8 presents retarded BEM simulations for the tomographically reconstructed bipyramid (Fig. 2). The spectra in Fig. S8b show similar features to the spectra for the ideal bipyramid in Fig. S7. The mesh, depicted in Fig. S8a, appears to be of sufficient quality for simulations down to 2 eV. Below the α signature energy the simulated loss probabilities become negative, an effect observed in MNPBEM simulations for imperfect surface meshes. The surface mesh was selected to sufficiently describe the experimental system without excessively increasing computational memory requirements. 6000 surface element retarded simulations approached 12 Gb. The $\xi_{2,3}$ features observed in Fig. S7 were also recorded in these BEM simulations, suggesting they do not arise from the particular surface mesh used for either Fig. S7 or S8. Rather, coupling effects with the truncated substrate or intrinsic challenges in meshing near the particle boundary likely give rise to these minor signals.

Mesh Generation

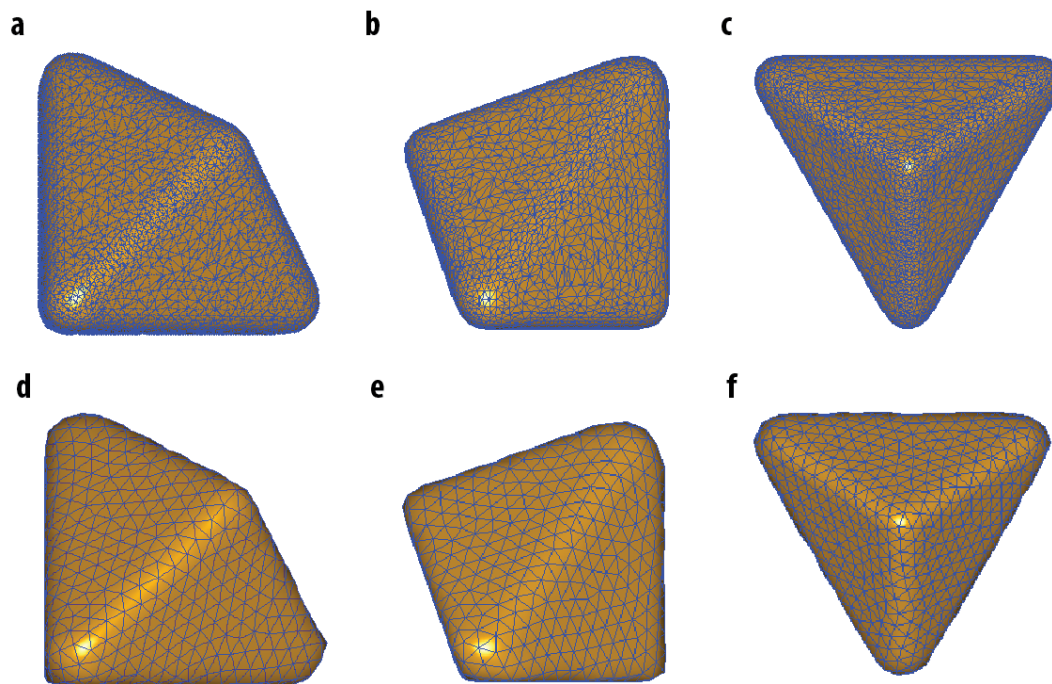


Figure S9 | Surface meshes for a thermodynamic bipyramid at multiple orientations. a-c, High quality surface mesh used for the simulation of theoretical surface charge distributions for bipyramid eigenmodes. **d-f,** Simplified surface mesh used for simulation of isolated bipyramid spectra (Fig. S5). Views highlighting the plan view orientation (**a, d**), the right angle characteristic of the right bipyramid (**b, e**) and the C_3 axis of the bipyramid (**c, f**) are shown for both surface meshes.

Figures S9 and S10 present additional views of the surface meshes generated for BEM simulations and for use in surface charge reconstructions. Figure S9 presents surface meshes used for isolated bipyramid simulations. Figure S9a-c present views along three orientations for a high-quality multi-level mesh of the isolated bipyramid surface generated using a Wulff construction method¹¹ and smoothed and meshed in AVIZO FIRE (see Methods). Figure S9d-f present views along three orientations along a simpler mesh of the Wulff thermodynamic bipyramid used for spectral simulations in Fig. S5. The orientations highlight the typical plan-

view orientation (a,d), a view perpendicular to the plan view perspective (b,e) emphasizing the right angle in the bipyramid, and a view along the three-fold (C_3) axis of the bipyramid (c,f).

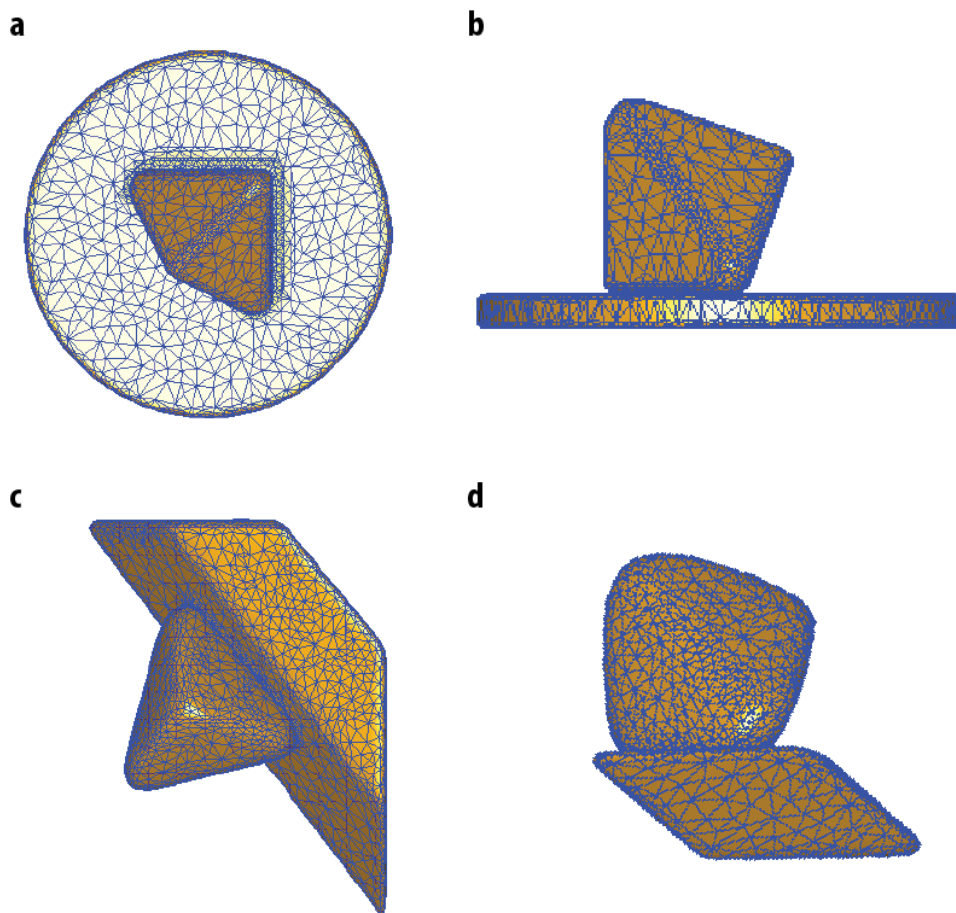


Figure S10 | Surface meshes for right bipyramids on dielectric substrates. a-b, Surface mesh used for simulation of a thermodynamic bipyramid on a dielectric substrate (plan view). **c-d,** Surface mesh derived from CS-ET of the bipyramid in Fig. 2. The right angle of the bipyramid is highlighted for both cases in **b, d**. The experimentally observed orientations, respectively plan view or at 0° tilt, are shown in **a, c**.

Figure S10 presents additional meshes for a bipyramid on a substrate. The mesh used for Fig. 1 and Fig. S7 is presented in Fig. S10a-b, and the mesh used for Fig. 2, Fig. S8, and for surface charge reconstructions (Fig. 5) is presented in Fig. S10c-d. For Fig. S10a-b, the typical plan-view orientation is shown alongside the corresponding orthogonal view (see Fig. S9b,e). For the tomographically reconstructed surface (Fig. S10c-d), the 0° tilt orientation, approximately along

the C_3 axis with a rotation in the orthogonal plane relative to Fig. S9c,f is shown as well as the corresponding cross-sectional view analogous to Fig. S10b and Fig. S9b,e. The significant truncation of the substrate volume is clarified in these representations of the surface mesh, and this truncation likely gives rise to the significantly higher energies of the modes simulated in Fig. S8 relative to those observed experimentally (0.7 eV for α peak, 0.4 eV for the β_1 peak, and less for higher energy features).

Tilt-series Bipyramid: NMF Decomposition

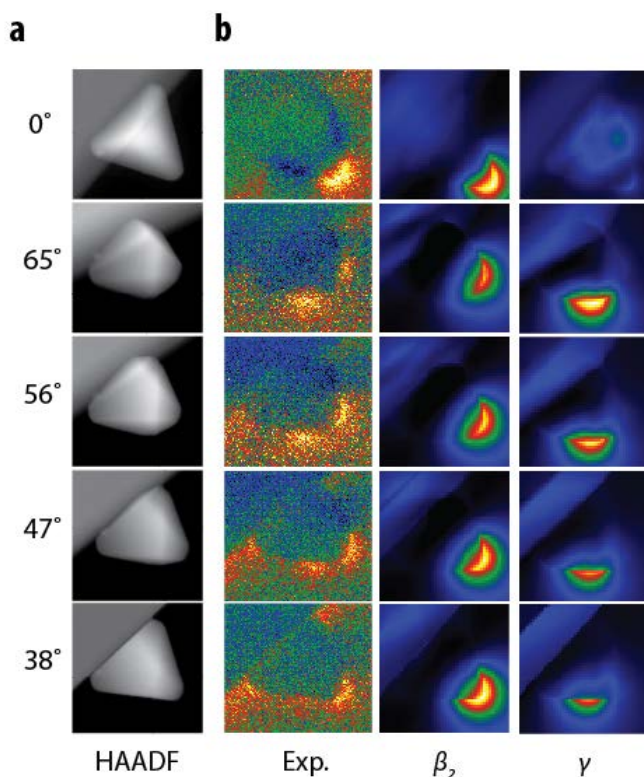


Figure S11 | Comparison of tilt-series EELS and simulations for $\beta_2+\gamma$ mode (Fig. 2). **a**, HAADF micrographs of silver right bipyramid on the MoO₃ substrate. **b**, NMF component map and loss probability maps simulated for each β_2 and γ spectral features. The maps are summed for comparison with the experimental NMF component map in Fig. 2.

Figures S11-13 present additional details of the NMF decomposition described in Fig. 2. Fig S11 shows the $\beta_2 + \gamma$ component from Fig. 2e alongside separate simulations for each the β_2 and γ peaks. The β_2 component exhibits lowest signal at high tilt angles (65°) with increasing

intensity toward 0° . The γ component exhibits greatest signal at high tilt and reduced intensity at lower angles. These trends are also observed in the experimental $\beta_2 + \gamma$ component maps.

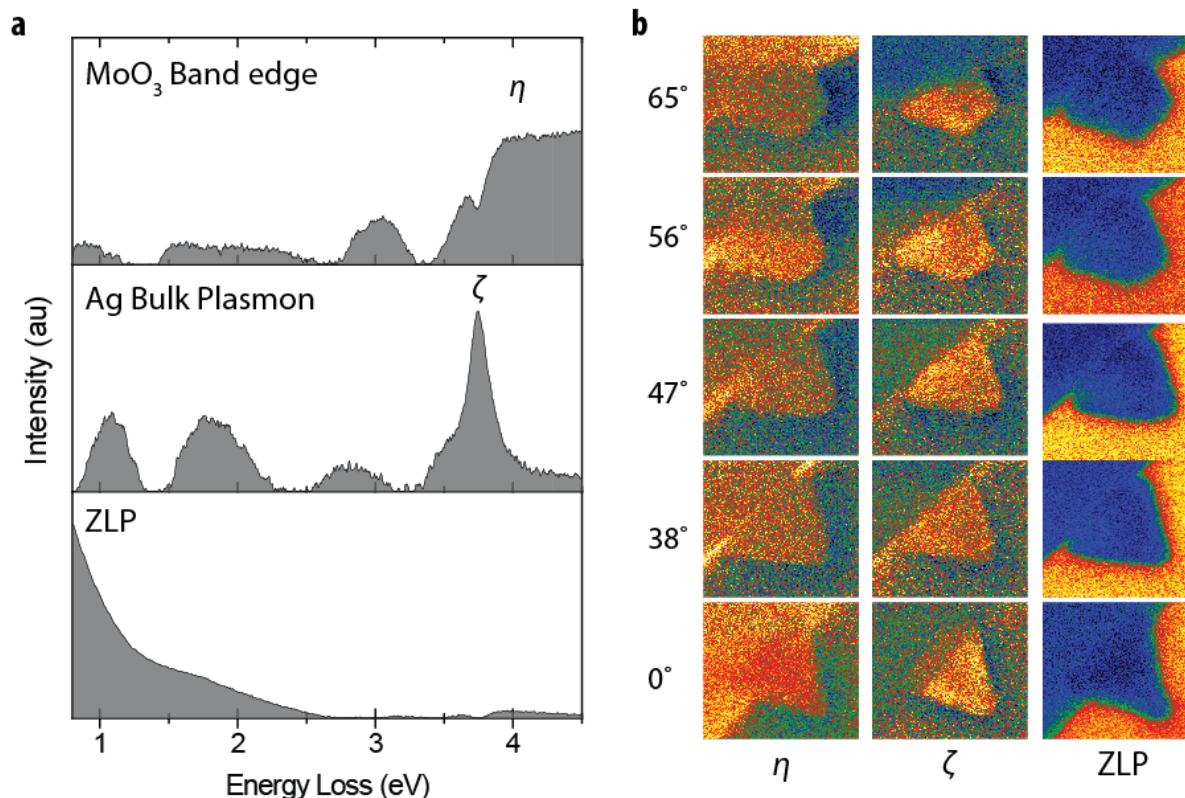


Figure S12 | Additional NMF components for the tilt-series decomposition (Fig. 2).

a, NMF spectral factors corresponding to the MoO₃ substrate band edge (η), Ag bulk plasmon (ζ), and the ZLP. **b**, Corresponding NMF component maps showing the intensity distribution for each spectral factor. The intensity scales are normalized for each map.

Figure S12 presents NMF components due to the MoO₃ band edge, silver (Ag) bulk plasmon, and ZLP for the decomposition described in Fig. 2. Whereas in Fig. 1 the ZLP spectral feature is incompletely separated from the MoO₃ feature, likely due to the equivalent distribution across the field of view for the substrate and the ZLP, in Fig. S12 the ZLP shows no significant similarity to the η feature. In this case, the spatial distributions of the substrate and ZLP vary, allowing NMF to separate the distinct signals. The MoO₃ band edge feature exhibits an intensity onset at approximately 3.5 eV as for the η feature for the plan-view bipyramid in Fig. 1, consistent with the bandgap of MoO₃.¹³ The component map in Fig. S12b shows intensity primarily in the substrate with low signal in vacuum. The signature is incompletely resolved

from the silver bulk plasmon feature as these overlap in energy. The Ag bulk plasmon (ζ) feature is observed as a strong peak at 3.8 eV. The dominant intensity in the component map is localized to the silver particle. For the feature, a smoothly decaying profile is observed in the spectral factor and relatively even intensity is observed in the component map.

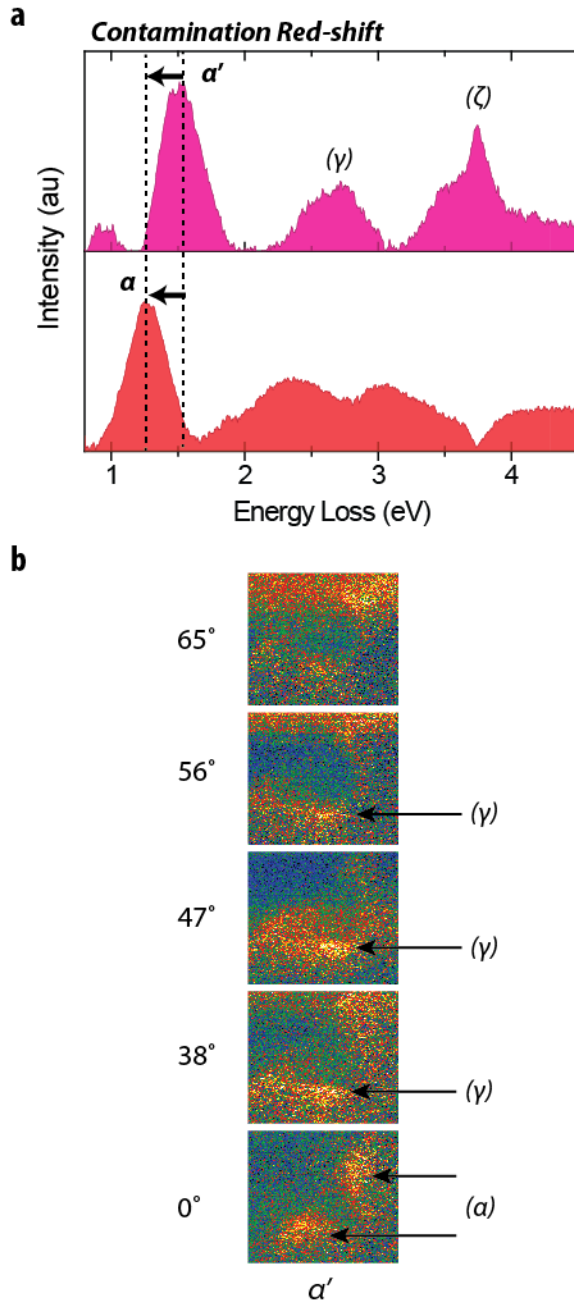


Figure S13 | Contamination-induced energy-shift component in NMF decomposition of tilt-series EELS. a, Comparison of an additional retained component accounting for energy-shift in the lowest corner mode and the dominant low-energy corner mode component (α). **b,** Corresponding NMF component maps for the 5 tilts used in mode analyses. Features corresponding to the shifted α (at 0° tilt, first experimental acquisition) and incompletely separated γ intensities are highlighted with arrows.

Figure S13 depicts the additional component retained in the NMF decomposition which describes a peak shift due to carbon contamination. This interpretation is established by inspection of the spectral factor and spatial component map for this additional component labeled α' . The spectral factor (Fig. S13a) shows a strong peak feature at approximately 1.5 eV, 0.2 eV higher in energy than the α component. Satellite features are also observed in the vicinity of the γ and ζ components. The component maps (Fig. S13b) reveal that the α' shows strong features attributable to the α signature expected from BEM simulations only for the 0° tilt-angle. At subsequent tilts the mapped features are dominated by repetition of the γ feature and some signal from the particle linked to the ζ volume plasmon spectral signature. Since the 0° tilt spectrum image was acquired first and represented the first extended electron beam exposure of the particle, carbon contamination deposited during the first spectrum image acquisition likely shifted the α spectral feature from 1.5 eV (α') to 1.3 eV as recovered in the α NMF component. As a result of this peak shift, the 0° tilt component maps were excluded for surface charge reconstructions of the corner modes. Sufficient pixels for reconstruction were available using four tilts only. The 0° tilt was included in the NMF decomposition to provide as much experimental signal as possible for decomposition analysis and to examine the effects of contamination from the first acquisition onward. Moreover, given that high order peaks show negligible energy shifts due to changing the dielectric environment (Fig. S5, S7), the NMF component maps for all five tilts were used for reconstructions involving the edge and face mode features (Fig. S17-20).

Eigenmode Calculations

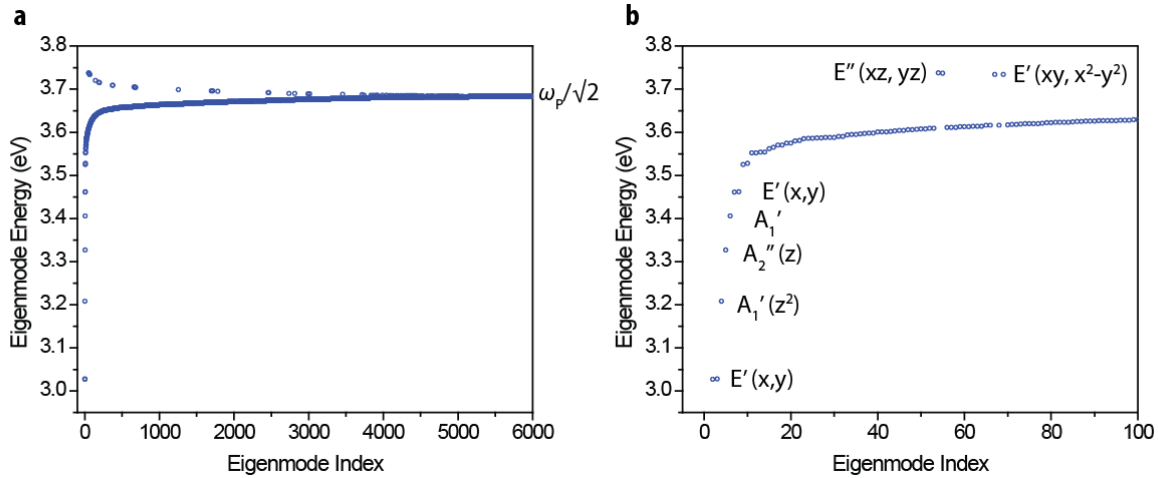


Figure S14 | Eigenmode energies for a thermodynamic silver right bipyramid. a, Eigenmode energies for all 6000 eigenmodes calculated with a 6000-element surface mesh (Fig. S9). **b,** First 100 eigenmodes with associated symmetry label indexing (see also Fig. 4).

Figure S14 plots the eigenmode energies for the modes depicted in Fig. 4. The eigenmodes are calculated using an eigenvalue solver in MATLAB. The eigenvalues are used to calculate the mode energies using the dielectric function for silver.¹⁴ The solver identifies modes approximately in order (mode index) of the multipolar order of the surface charge distribution. That is, the first (index 1) mode is one of the dipole modes of the $E'(x,y)$ set. Inspection of the surface charge distributions (eigenvectors) determined by the solver confirmed the simultaneous increase in multipolar order of the surface charge mode and the index of the mode identified by the eigenvalue solver. Here, the multipolar order is understood in terms of the spatial frequency of surface charge oscillations. As the eigenmode index tends toward 6000, the surface charges oscillate with increasing frequency. The modes with energies above 3.68 eV (corresponding to the accumulation point at $\omega_p/\sqrt{2}$ for Ag) are identified as the face modes. The modes below 3.68 eV are identified as corner modes (lowest energy) and edge modes (higher energy). The accumulation point here refers to the convergence of the face and edge mode energies for the bipyramid. There is no distinction between edge and face modes as the mode order increases as very high order multipolar modes are characterized by high spatial frequencies in surface charge oscillations and so there are no longer clear charges distributed across the faces or confined along an edge as in the case of the lowest order modes in these series (Fig. 4). This accumulation

point is identical to that observed in plasmonic metal spheres.^{12,15} In the case of spheres, this accumulation point is also well-known as the energy of a surface plasmon polariton of a metal plane as at high multipolar mode order for spheres the high frequency of the charge oscillations on the surface behave electromagnetically as if without the surface curvature.¹²

Validation of Corner Mode Reconstructions

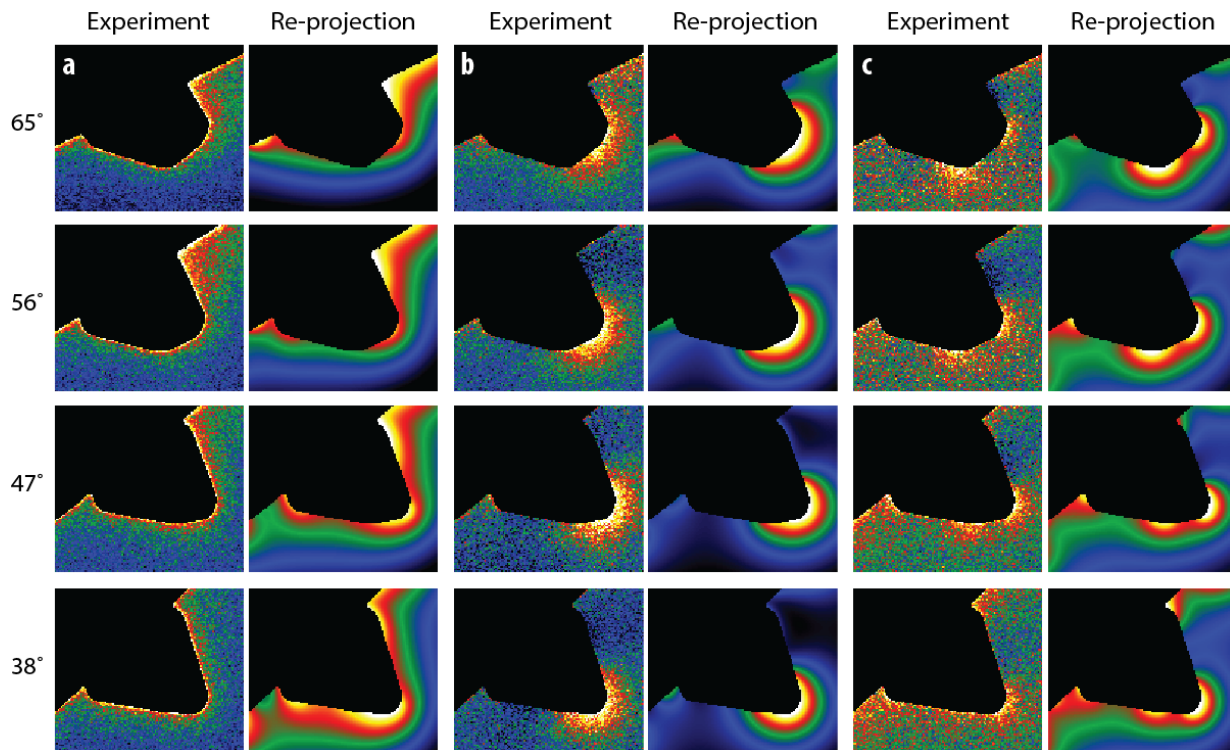


Figure S15 | Masked experimental EELS and re-projections of simulated EELS for the corner modes of a silver right bipyramid. Modes for the x-dipole (a), y-dipole (b), and the combination of the z^2 -quadrupole and z-dipole (c) are shown at the 4 tilts used to analyze the corner modes. Maps are each plotted on a normalized intensity scale for easy comparison of each pair (experimental, re-projection).

Figure S15 presents a comparison of experimental NMF component maps and modal loss probability maps re-calculated from the surface charge reconstructions presented in Fig. 5. Penetrating trajectories are masked and appear black as these were not used in the surface charge reconstruction. These re-calculated loss probability maps show good correspondence with the experimental component maps. They exhibit smoother intensity distributions, constrained by the ϕ^* term in equation (1). The effects of minor artefacts in the experimental component maps are

also reproduced, demonstrating the reconstruction algorithm identifies solutions to maximize fidelity with the experimental data. For Fig. S15a, the asymmetric intensity distribution from left to right at 65° and 56° is reproduced in the re-calculated maps. This intensity becomes more symmetric around the entire particle for 47° and 38° . In Fig. S15b-c, the intensity at the vacuum-substrate interface in the top-right corner at 65° is reproduced in the reconstruction map. These features can be seen in the surface charge reconstructions as the surface charge in the substrate away from the particle. These re-projections also validate the use of the truncated substrate. The bipyramid on the partial substrate used for the mesh (in contrast with the extended substrate in the experimental set-up) gives rise to comparable intensity distribution maps for the reconstructed corner modes.

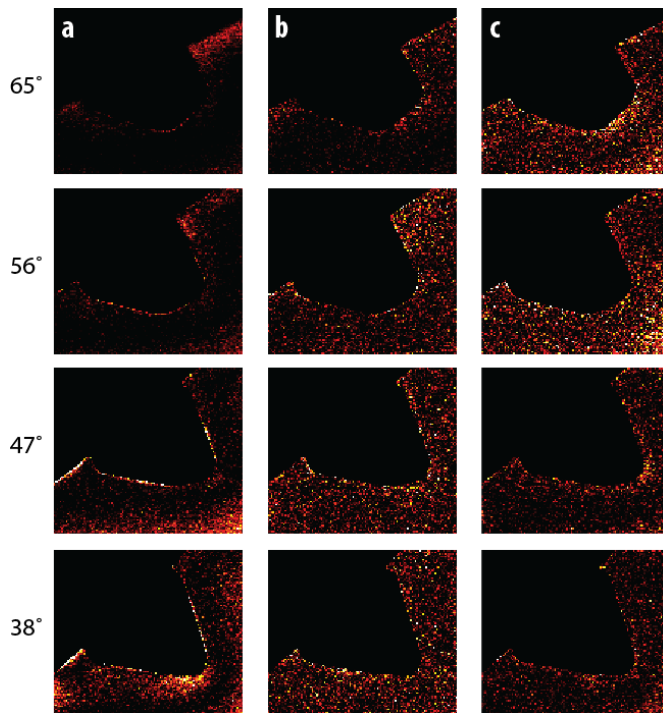


Figure S16 | Maps of the data fidelity term J contributions at each pixel for reconstructed corner modes. Modes for the x-dipole (a), y-dipole (b), and the combination of the z^2 -quadrupole and z-dipole (c) are shown at the 4 tilts used to analyze the corner modes. Maps are plotted on a self-consistent intensity scale within each column.

To further examine the solutions for surface charge distributions (Fig. 5) and the corresponding re-projections (Fig. S15), plots of the data fidelity term J (see equation (4)) contributions at each pixel are presented in Fig. S16 for the three corner mode NMF component

maps. For the lowest energy corner mode α (x-dipole), there are particular regions giving rise to residual differences with the experimental data, principally along the edges of the particle in the 56° and 47° maps, the tip in vacuum in the 38° map, and a region along the substrate in the 65° , 47° , and 38° maps. As noted, the α component is most severely affected by contamination and so inconsistencies within the data set result in differences between the re-projection and experimental data that cannot be resolved by a single solution of the surface charge reconstruction. The observation that these residual differences contributing to J are increasingly large at subsequent tilts in time is consistent with contamination effects. In comparison, the β_1 (y-dipole), and $\beta_2+\gamma$ (z^2 -quadrupole and z-dipole) maps show relatively even contributions to J throughout the map with slightly higher contributions immediately adjacent to the particle surface, attributed to slight misalignments of the tomographically reconstructed surface and the true particle (see also Fig. S21-S22).

Edge and Face Mode Reconstructions

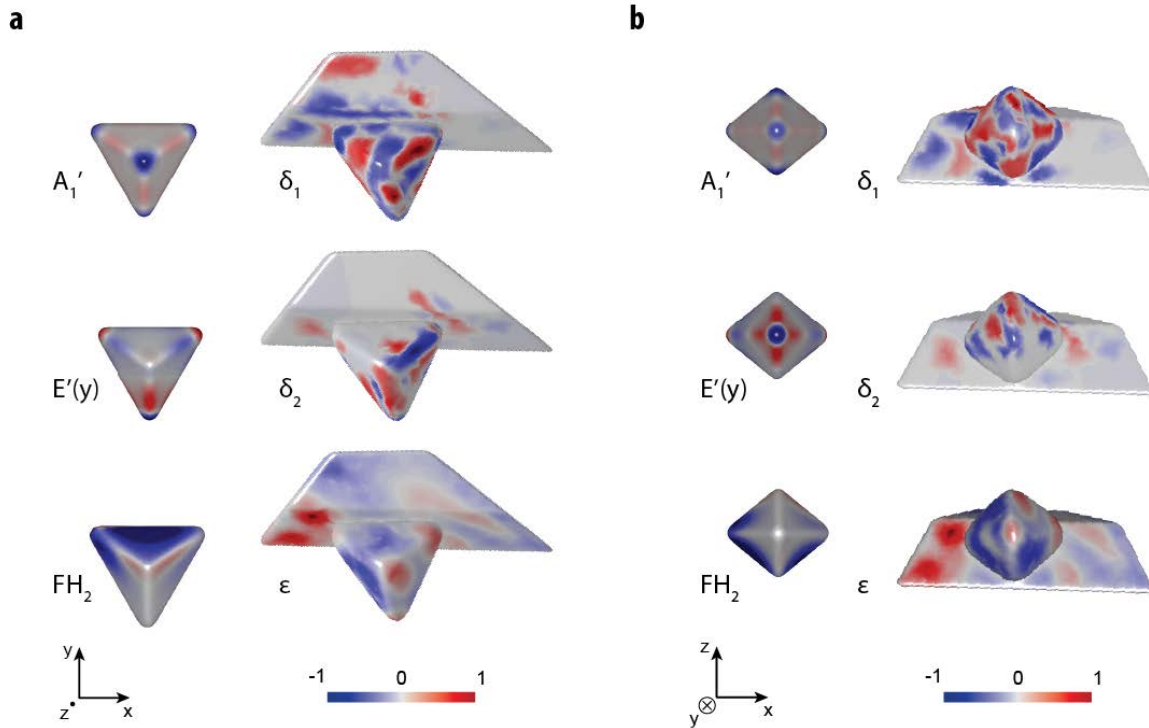


Figure S17 | Dominant eigenmode contributions to edge and face modes and corresponding surface charge reconstructions for a silver right bipyramid on a MoO₃ dielectric substrate. a-b, For each eigenmode, one orientation along the C₃ (z) axis of the bipyramid (**a**) and one perpendicular orientation (**b**) are shown corresponding to the indicated coordinate axes. The color scale is normalized for each mode. Greek letters refer to the NMF component used for the reconstruction. Symmetry labels are given for an isolated bipyramid (*D*_{3h} point group). The designation FH₂ refers to the second hybrid face eigenmode for a system including symmetry breaking (See Fig. S18).

In Fig. S17-20, the surface charge tomography approach is extended to the edge and face mode series. For these mode series, where multiple higher order modes partially contribute (see Fig. S14), it is not possible to obtain reconstructions of pure modes as required for a simple application of equations (1)-(2). Instead, only the dominant contribution to the experimental signal can be reconstructed using a partial sum over modes. The number of modes to include and initial guesses to start the refinement using the conjugate gradient algorithm required exploration of several combinations of modes. Fig. 4 predicts that the lowest order edge modes comprise an A₁' mode and two modes deriving from a degenerate pair. For the face modes, two pairs of degenerate modes are expected for an isolated bipyramid. Low order modes are likely to

dominate the experimental spectrum for small particles.¹² Reconstructions for edge and face modes were repeated for different sets of initial guesses and for varied truncation of the series with 1-4 modal contributions. More than four modes could not be reconstructed with confidence with experimental data due to the finite number of pixels available for reconstruction.

Ultimately, two major contributions were identified to the edge mode feature δ and one contribution was identified for the face mode feature ε that could be traced to simulated eigenmodes of the bipyramid (see also Fig. 4). Figure S17 depicts surface charge reconstructions for these dominant contributions observed in available experimental data.

For the edge modes, attempts to reconstruct a single mode from experimental data failed to offer charge distributions consistent with expected low-order edge modes. Rather, a two-mode reconstruction recovered modes bearing resemblance to the A_1' edge mode (δ_1) and the y-component of the E_1' mode (δ_2). Although the x-component of the E_1' edge mode is expected at lower energy as it is localized to the substrate (Fig. 5), experimental tilt series data of non-penetrating trajectories contain more information about the y-component than the x-component. Consistently, the reconstructions reflect the most intense EELS measurements recorded, those with high surface charge and associated potentials in the vacuum. It is also possible that the x-component and y-component of the degenerate pair of edge modes in the ideal isolated bipyramid undergo symmetry breaking not only due to the substrate but due to the varyingly sharp corners (see also asymmetry in α feature and the corresponding x-dipole mode). A degenerate pair in the isolated bipyramid may split into any two linear combinations of the degenerate pair as determined by the new broken symmetry of the system. The edge mode identified as similar to y-component may in fact be a linear combination of the x-component and y-component of the ideal isolated bipyramid.

For face modes, the substrate-induced symmetry breaking has a major effect on modal surface charge distributions (see Fig. S18). Figure S18 presents eigenmode calculations for a model system of a dielectric disk near an ideal bipyramid. The disk was positioned in space to mimic the symmetry breaking of the substrate in the tilt-series experiment (Fig. 2). The disk and bipyramid were separated by vacuum (4 nm separation at the closest point between the particle and substrate meshes) to avoid any simulation artefacts due to meshing a shared surface boundary. Figure S18a displays the mesh used for these eigenmode calculations. Figure S18b presents the eigenmode energies, highlighting the face modes. With the disk, the degeneracy of

the isolated bipyramid modes is removed. Similar symmetry breaking-induced degeneracy loss was likewise observed for the corner and edge modes using this model system. The surface charge distributions corresponding to the lowest order face mode in the low-symmetry model system are displayed in Fig. S18c. The charge distributions resemble distributions of the isolated bipyramid but are modified, attributed to mode hybridization and mixing as observed in other plasmonic systems.^{14,16}

For experimental reconstructions, reconstructions for 1-4 modes were attempted using the symmetries of the modes of the ideal bipyramid and their linear combinations as initial guesses. These reconstructions, however, resulted in optimized solutions that bore little resemblance to either the isolated bipyramid modes or those of the symmetry-broken system in Fig. S18. Closest agreement with mode symmetries observed in Fig. S17 were instead found for a reconstruction of a single mode from randomly initialized surface charge on the bipyramid. This reconstruction (Fig. S17), labeled Face Hybrid 2 (FH₂, ii. in Fig. S18c) has negative charge on the faces (blue) and an asymmetric positive charge distribution along the axial corner (Fig. S17). In the simulated FH₂ mode, there is also very low valued positive charge along the equatorial edges and the equatorial corner away from the substrate (Fig. S18). These positive charges appear more strongly in the experimental reconstruction; the surface charge distribution for the experimental particle is further modified by the particular substrate and particle geometry. Clear eigenmode calculations were not possible using the experimental particle mesh due to abrupt jumps in the surface mesh which are problematic for the MNPBEM implementation.¹⁰ Although agreement between the experimental and simulated eigenmode surface charge distributions in Fig. S17 is imperfect, these reconstructions assist in identifying the major mode contributions to these higher order multipolar mode series. These reconstructions are intrinsically limited by the overlap of multiple higher order modes.

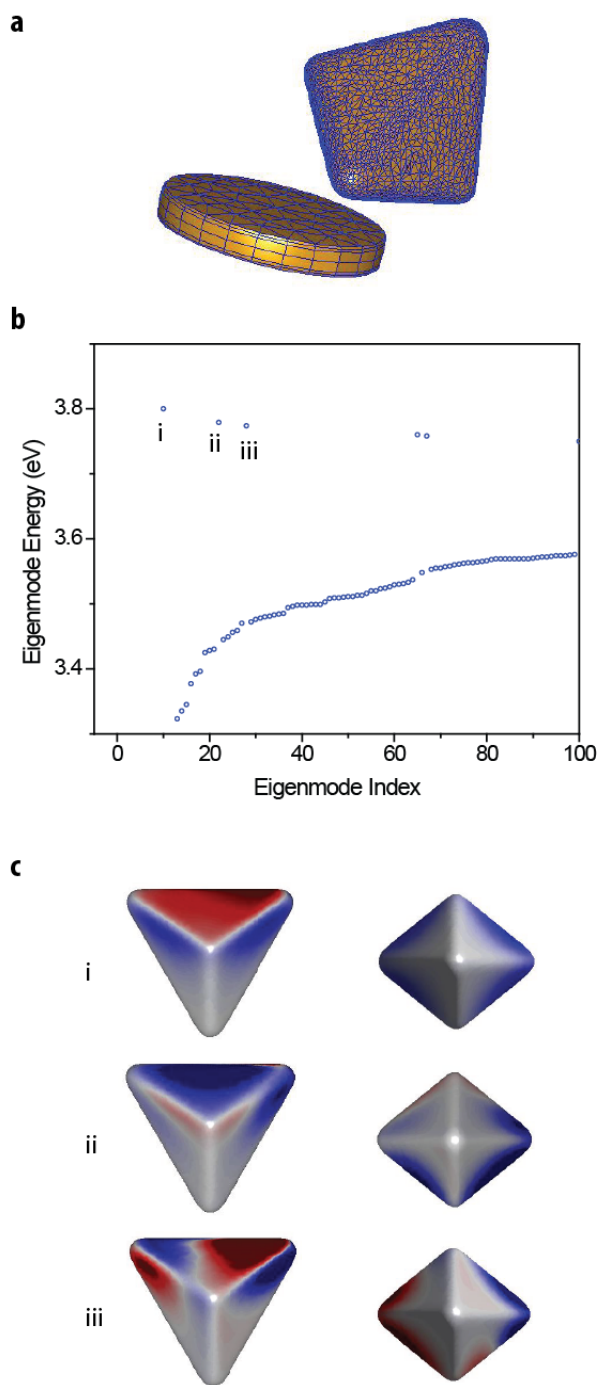


Figure S18 | Eigenmode energies of the lowest order face modes of a silver right bipyramid with symmetry breaking. **a**, Surface mesh of the symmetry-breaking system. The disk is the dielectric material as for the modeling of the MoO₃ substrate. **b**, Eigenmode energies (i-iii) for the three lowest order face modes. **c**, Surface charge distributions on the silver bipyramid in the symmetry-breaking model system. Surface charges are plotted on an intensity scale to highlight the symmetry of the charge distribution.

Recalculated loss probability maps (Fig. S18) for the reconstructions in S16 confirm that the reconstructions reproduce EELS intensity distributions consistent with the recorded data. As for the corner modes (Fig. S15), the re-calculated loss probability maps from reconstructed surface charges exhibit somewhat more continuous decay into vacuum than the experimental reconstructions. However, the signal distribution at all five tilts closely follows the intensities observed experimentally. That is, there is a direct correspondence between signal features in the experimental NMF component maps and features in the re-calculated maps. The face mode, as for some corner modes, also exhibits signal along the substrate-vacuum boundary which is in turn manifested in the surface charges placed on the substrate away from the immediate vicinity of the bipyramid. While these signals cannot be attributed to the surface plasmon resonance modes of the silver bipyramid, they do verify that the reconstruction algorithm places charges in accordance with experimental data and is not overly restricted by regularization parameters or by the choice of the initial guess. The majority of intensity in the experimental maps is accounted for by the surface mode reconstructions. This correspondence validates the reconstructions as a reasonable description of available experimental data for predicting the optical response of the silver right bipyramid.

As with the corner modes, Fig. S20 also presents the pixel-by-pixel contributions to the data fidelity term J . The highest contributions occur in the immediate vicinity of the particle surface, attributed to imperfections in experimental data alignment with the reconstructed surface mesh. These mostly single-pixel misalignments likely more strongly affect edge and face modes where the intensity in the EELS maps is highly localized to the immediate vicinity of the particle surface. The face mode also gives rise to strong contributions to J for the 0° map along the edges of the particle surface. In this case, contamination after the acquisition of the 0° experimental map likely gave rise to a self-inconsistency in the face mode tilt series and so the single solution of surface charges cannot perfectly match the high intensities at the edge of the particle in the 0° map simultaneously with the other tilt data.

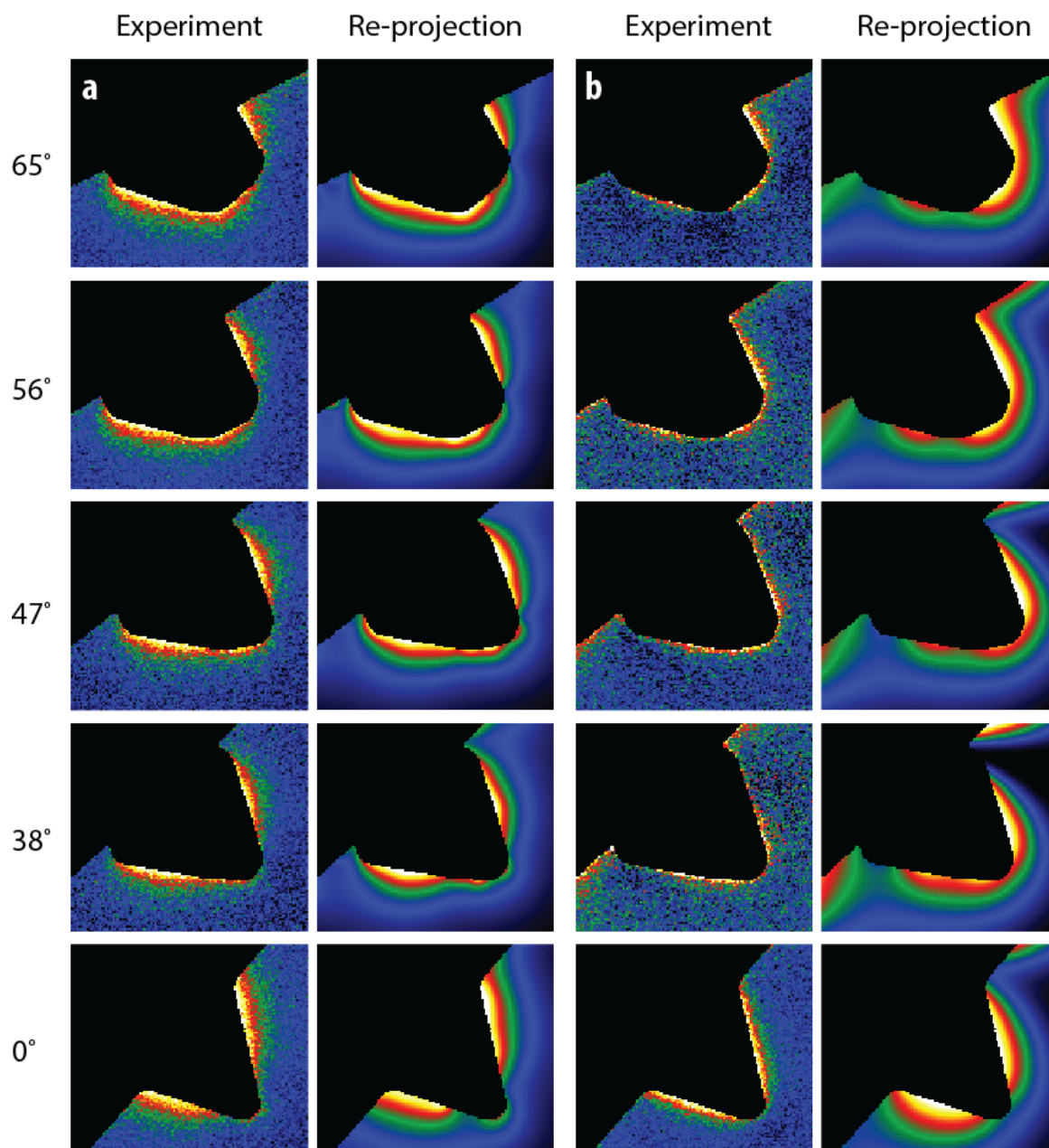


Figure S19 | Masked experimental EELS and re-projections of simulated EELS for the edge and face modes of a silver right bipyramid. Modes along the edges (**a**) and faces (**b**) are shown at the 5 tilts used to analyze these modes. Maps are each plotted on a normalized intensity scale for easy comparison of each pair (experimental, re-projection).

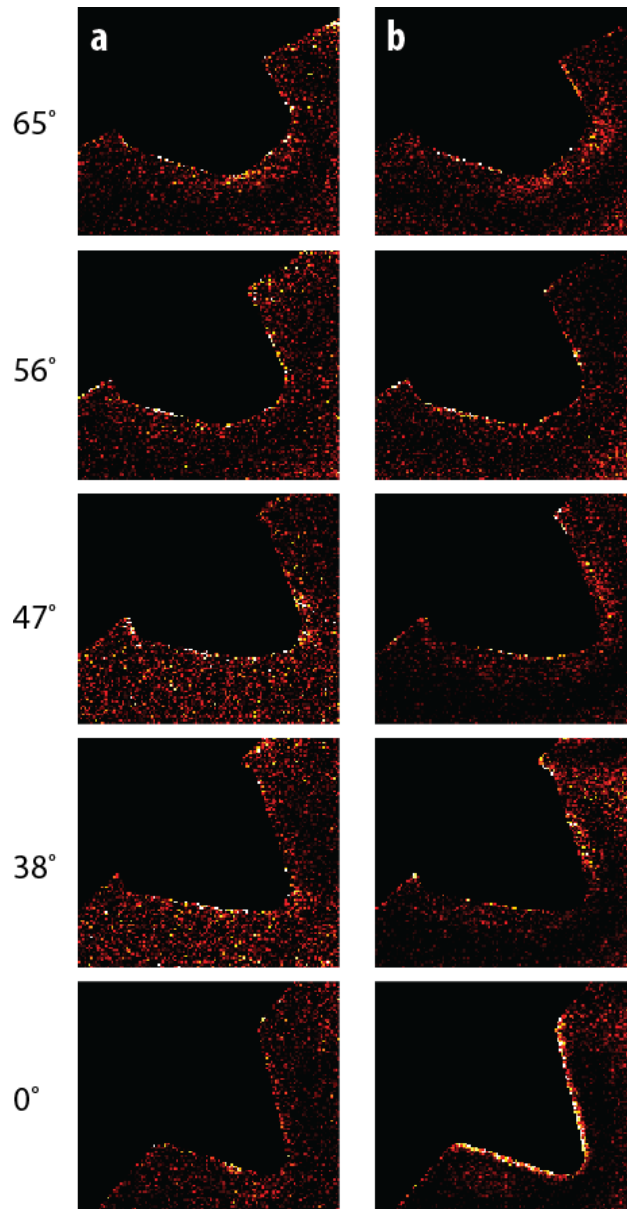


Figure S20 | Maps of the data fidelity term J contributions at each pixel for reconstructed edge and face modes. Modes along the edges (**a**) and faces (**b**) are shown at the 5 tilts used to analyze these modes. Maps are plotted on a self-consistent intensity scale within each column.

Phantom Calculations

Finally, Fig. S21-S23 present additional calculations to test the validity of the reconstruction algorithm. These calculations use simulated retarded BEM energy loss probabilities at the experimentally determined beam trajectories as the input for reconstruction. This approach is analogous to phantom reconstruction calculations typical in validating tomographic reconstruction methods. The y -dipole β_1 feature was selected for this demonstration.

In Fig. S21, the retarded BEM loss probabilities for the same five tilts used for NMF decomposition are presented alongside re-calculated (re-projection) maps and data fidelity maps for an initial guess consisting of randomly selected charges within a symmetric range centered on zero and maps calculated from the final output of the reconstruction algorithm. The random charge initialization (guess) bears little resemblance to the retarded BEM simulation data (Phantom data). The data fidelity J -contribution map in turn is dominated by the differences where the phantom data is most intense and so bears close resemblance to the phantom data. After reconstruction, the re-projections resemble the phantom data maps and the data fidelity maps show significant contributions exclusively localized to where there are 1-2 pixel offsets in the experimental maps and the tomographically reconstructed particle surface. As these highlight sub-regions of the particle surface (i.e. the contributions to J do not form a continuous line around the particle surface) these highlight 1-2 pixel deviations between the segmented tomogram obtained from tilt-series ADF imaging and the particle surface in each of the acquired EELS maps.

The corresponding surface charge distributions for the random initialization are presented in Fig. S23a-b. This set of reconstructions highlights the ill-posed nature of the reconstruction problem, in that the re-projections are brought into resemblance with the available experimental data but there remains a highly unphysical and high spatial frequency oscillation of surface charge along the particle surface. Inspection of Fig. S23b suggests concentrations of positive (red) charge at the proximal corners and negative (blue) charge at the corner in vacuum, consistent with approaching an expected y -dipole charge distribution. The remaining fine-scale charges across the particle surface do not, however, contribute enough to the gradient of J to promote further optimization. In fact, numerical precision loss ultimately terminated the reconstruction when a lower tolerance on the norm of the gradient of 1×10^{-7} was selected for the random initialization reconstruction.

Fig. S22 presents similar phantom reconstruction calculations using an eigenmode initial guess and only four tilts as used in the processing of experimental data. The eigenmode initial guess exhibits generally similar spatial distributions of intensity near the particle corner and surfaces as in the retarded BEM simulation phantom data. After reconstruction, the re-projection maps show improved agreement with the phantom data in accord with the goal of the reconstruction algorithm. As for the random initialization, the contributions to J are almost exclusively localized to a 1-2 pixel region where the tomographically reconstructed surface imperfectly matches the particle surface in the experimental EELS maps. The fidelity of the structural surface reconstruction from the ADF tilt series may ultimately limit the accuracy of the reconstruction method in this case.

Figures S23c-d present the corresponding initial and final surface charge distributions. For the initial surface charges, the substrate effects are not taken into account. For the final surface charge distribution, the charge distribution remains smoothly varying and does not exhibit the effects of rapidly varying local surface charge as in the random initialization. These charges show much greater resemblance to the single particle eigenmode charges both in distribution on the particle and the smooth decay from the corners. The substrate charges appear to be of the same sign immediately in the vicinity of the proximal corners which differs from the experimentally reconstructed surface charges for the y -dipole (β_1). The difference may be attributed to the finite v. effectively infinite substrate in the experimental case or to background from other contributing modes in the phantom data as the phantom data as calculated for a single energy near the β_1 -resonance but without separation of overlapping peaks. In any case, the phantom calculations highlight the importance of selecting a reasonable guess for refining surface charge distributions using a limited tilt-range. The requirement to initialize the reconstruction algorithm with a guess of the correct symmetry was noted previously,² but these calculations demonstrate the reconstruction algorithm performance as implemented with the experimental data presented here.

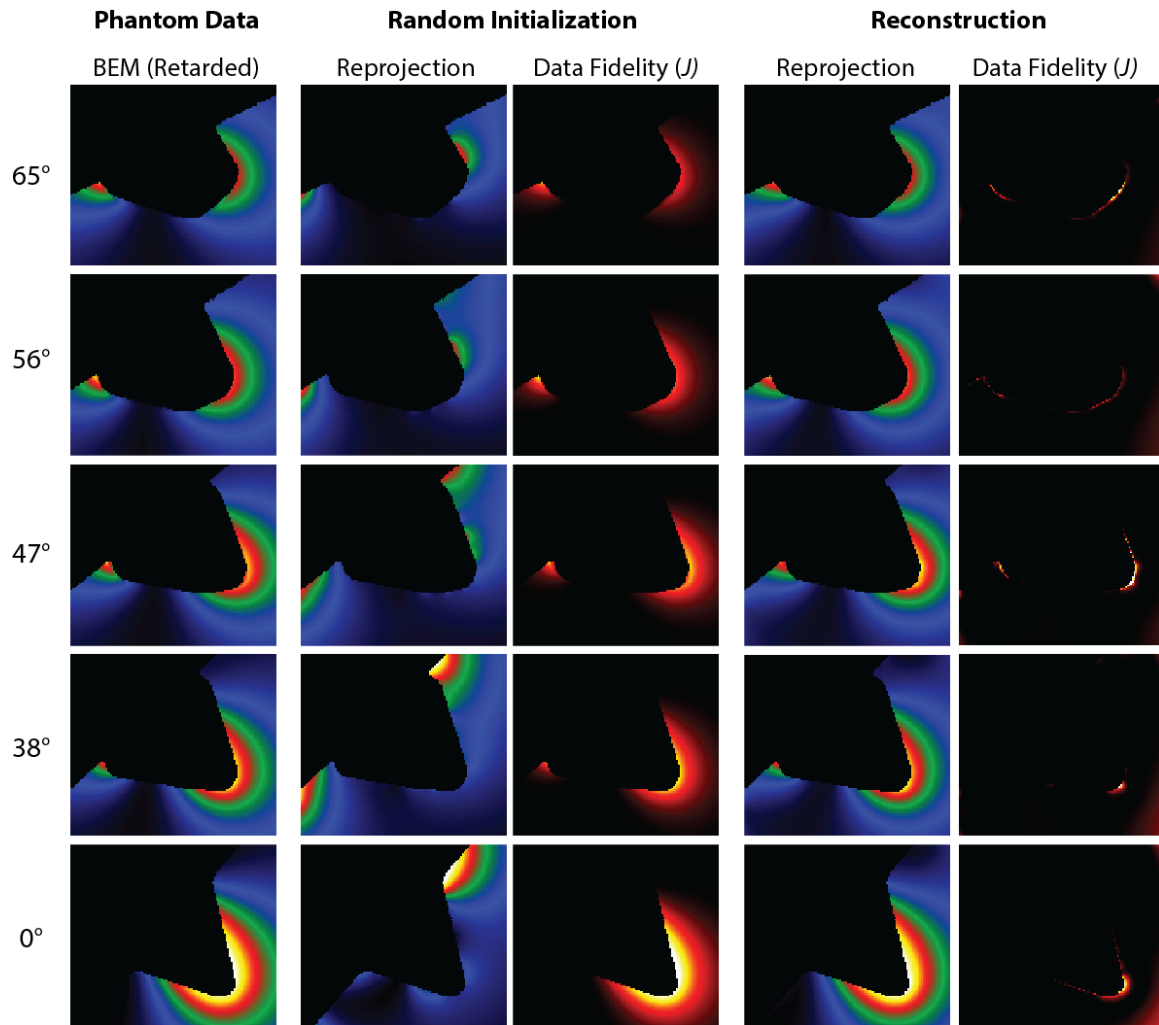


Figure S21 | Phantom testing using random initialization of surface charges. The phantom data (retarded BEM simulation at experimental trajectories) as well as reprojections and maps of the data fidelity term J are shown for the initial charge distribution and the reconstructed charge distribution. Maps are plotted on a self-consistent intensity scale within each column.

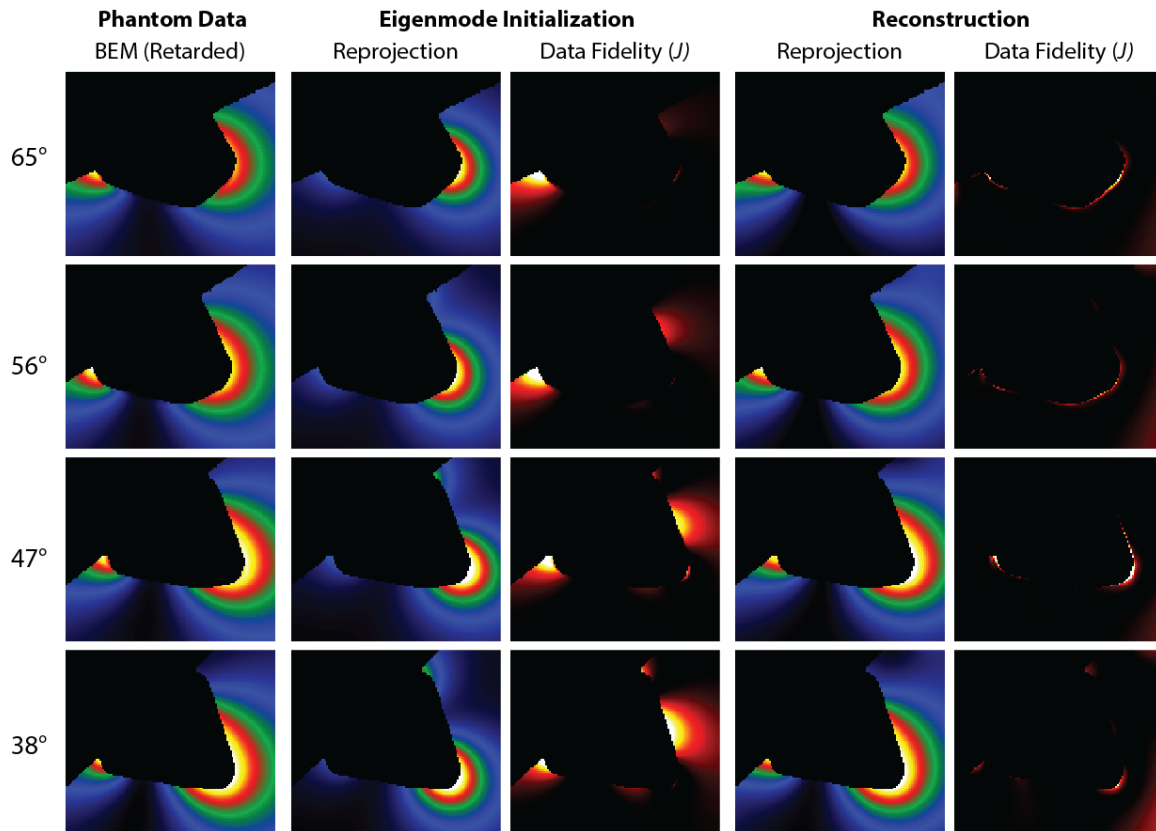


Figure S22 | Phantom testing using eigenmode initialization of surface charges. The phantom data (retarded BEM simulation at experimental trajectories) as well as reprojections and maps of the data fidelity term J are shown for the eigenmode initialization and the reconstructed charge distribution. Maps are plotted on a self-consistent intensity scale within each column.

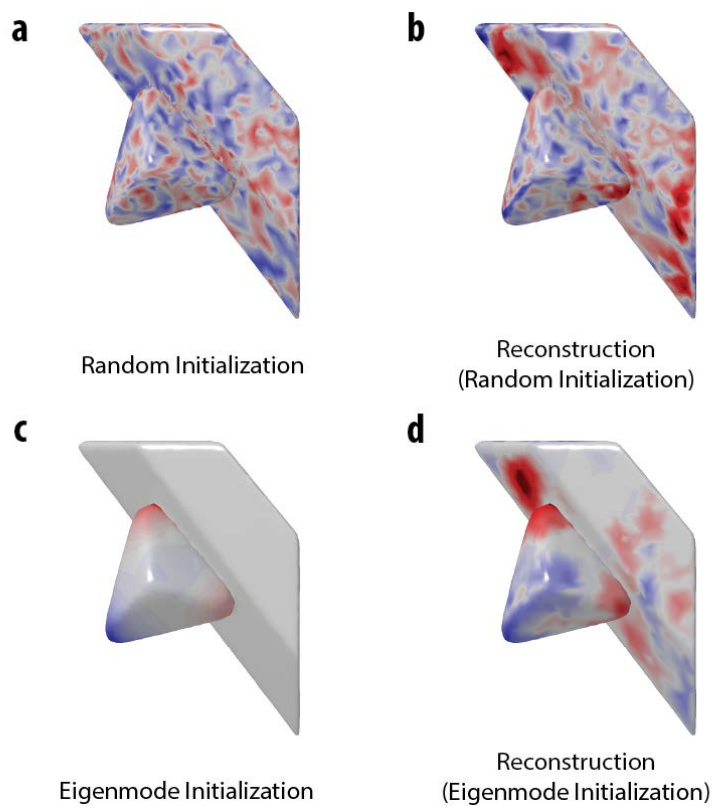


Figure S23 Surface charge distributions used in re-projections in Fig. S20-21. The surface charge distributions for the random initialization, reconstruction from the random initialization, as well as the reconstruction from the eigenmode initialization are shown.

References

- (1) Nicoletti, O.; de la Peña, F.; Leary, R. K.; Holland, D. J.; Ducati, C.; Midgley, P. A. *Nature* **2013**, *502* (7469), 80–84.
- (2) Hörl, A.; Trügler, A.; Hohenester, U. *Phys. Rev. Lett.* **2013**, *111* (7), 076801.
- (3) Hörl, A.; Trügler, A.; Hohenester, U. Full three-dimensional reconstruction of the dyadic Green tensor from electron energy loss spectroscopy of plasmonic nanoparticles. Personal Communication, 2015.
- (4) Calvetti, D.; Morigi, S.; Reichel, L.; Sgallari, F. *J. Comput. Appl. Math.* **2000**, *123* (1–2), 423–446.
- (5) Saghi, Z.; Holland, D. J.; Leary, R.; Falqui, A.; Bertoni, G.; Sederman, A. J.; Gladden, L. F.; Midgley, P. A. *Nano Lett.* **2011**, *11* (11), 4666–4673.
- (6) Leary, R.; Saghi, Z.; Midgley, P. A.; Holland, D. J. *Ultramicroscopy* **2013**, *131*, 70–91.
- (7) Candes, E. J.; Romberg, J.; Tao, T. *IEEE Trans. Inf. Theory* **2006**, *52* (2), 489–509.
- (8) Lustig, M.; Donoho, D.; Pauly, J. M. *Magn. Reson. Med.* **2007**, *58* (6), 1182–1195.
- (9) Donoho, D. L. *IEEE Trans. Inf. Theory* **2006**, *52* (4), 1289–1306.
- (10) Hohenester, U. *Comput. Phys. Commun.* **2014**, *185* (3), 1177–1187.
- (11) Ringe, E.; Van Duyne, R. P.; Marks, L. D. *J. Phys. Chem. C* **2013**, *117* (31), 15859–15870.
- (12) Rivacoba, A.; Zabala, N.; Aizpurua, J. *Prog. Surf. Sci.* **2000**, *65* (1), 1–64.
- (13) Deb, S. K. *Proc. R. Soc. Lond. Ser. Math. Phys. Sci.* **1968**, *304* (1477), 211–231.
- (14) Schmidt, F. P.; Ditlbacher, H.; Hofer, F.; Krenn, J. R.; Hohenester, U. *Nano Lett.* **2014**, *14* (8), 4810–4815.
- (15) Collins, S. M.; Midgley, P. A. *Phys. Rev. B* **2013**, *87* (23), 235432.
- (16) Zhang, S.; Bao, K.; Halas, N. J.; Xu, H.; Nordlander, P. *Nano Lett.* **2011**, *11* (4), 1657–1663.